A warm Neptune's methane reveals core mass and vigorous atmospheric mixing

David K. Sing[1,2]✉ , Zafar Rustamkulov[1], Daniel P. Thorngren[2], Joanna K. Barstow[3], Pascal Tremblin[4,5], Catarina Alves de Oliveira[6], Tracy L. Beck[7], Stephan M. Birkmann[6], Ryan C. Challener[8], Nicolas Crouzet[9], Néstor Espinoza[7], Pierre Ferruit[6], Giovanna Giardino[10], Amélie Gressier[7], Elspeth K. H. Lee[11], Nikole K. Lewis[8], Roberto Maiolino[12], Elena Manjavacas[2,13], Bernard J. Rauscher[14], Marco Sirianni[15] and Jeff A. Valenti[7]

[1]Department of Earth & Planetary Sciences, Johns Hopkins University, Baltimore, MD, 21218, USA. [2]Department of Physics & Astronomy, Johns Hopkins University, Baltimore, MD, 21218, USA. [3]School of Physical Sciences, The Open University, Milton Keynes MK7 6AA, UK. [4]Université Paris-Saclay, UVSQ, CNRS, CEA, Maison de la Simulation, F-91191 Gif-sur-Yvette, France. [5]Université Paris-Saclay, Université Paris Cité, CEA, CNRS, AIM, 91191 Gif-sur-Yvette France. [6]European Space Agency, European Space Astronomy Centre, 28692 Villanueva de la Canada, Madrid, Spain. [7]Space Telescope Science Institute, Baltimore, MD 21218, USA. [8]Department of Astronomy and Carl Sagan Institute, Cornell University, Ithaca, NY, 14853, USA. [9]Leiden Observatory, Leiden University, P.O. Box 9513, 2300 RA Leiden, The Netherlands. [10]ATG Europe for the European Space Agency, ESTEC, Noordwijk, The Netherlands. [11]Center for Space and Habitability, University of Bern, Gesellschaftsstrasse 6, CH-3012 Bern, Switzerland. [12]University of Cambridge, The Old Schools, Trinity Ln, Cambridge CB2 1TN, UK. [13]AURA for the European Space Agency (ESA), ESA Office, Space Telescope Science Institute, 3700 San Martin Drive, Baltimore, MD, 21218 USA. [14] NASA Goddard Space Flight Center, Greenbelt, MD 20771, USA. [15]European Space Agency (ESA), ESA Office, Space Telescope Science Institute, 3700 San Martin Drive, Baltimore, MD 21218, USA. ✉email: dsing@jhu.edu.

Observations of transiting gas giant exoplanets have revealed a pervasive depletion of methane[1,2,3,4], which has only recently been identified atmospherically[5,6]. The depletion is thought to be maintained by disequilibrium processes such as photochemistry or mixing from a hotter interior[7,8,9]. However, the interiors are largely unconstrained along with the vertical mixing strength and only upper limits on the CH_4 depletion have been available. The warm Neptune WASP-107 b stands out among exoplanets with an unusually low density, reported low core mass[10], and temperatures amenable to CH_4 though previous observations have yet to find the molecule[2,4]. Here we present a JWST NIRSpec transmission spectrum of WASP-107 b which shows features from both SO_2 and CH_4 along with H_2O, CO_2, and CO. We detect methane with 4.2σ significance at an abundance of 1.0±0.5 ppm, which is depleted by 3 orders of magnitude relative to equilibrium expectations. Our results are highly constraining for the atmosphere and interior, which indicate the envelope has a super-solar metallicity of 43±8× solar, a hot interior with an intrinsic temperature of T_{int}=460±40 K, and vigorous vertical mixing which depletes CH_4 with a diffusion coefficient of $K_{zz} = 10^{11.6\pm0.1}$ cm^2/s. Photochemistry has a negligible effect on the CH_4 abundance, but is needed to account for the SO_2. We infer a core mass of $11.5^{+3.0}_{-3.6}$ $M_\oplus$, which is much higher than previous upper limits[10], releasing a tension with core-accretion models[11].

We observed one transit of the exoplanet WASP-107 b[12] with JWST NIRSpec's G395H spectral grating as part of Guaranteed Time Observations (GTO) program 1224 (P.I. Birkmann). In JWST's first years of operation, this mode demonstrates reliable detections of H_2O, CO, CO_2 and SO_2 for a number of giant exoplanets[7,17,18,19]. See the Methods for further details regarding the observations and data analysis. The wavelength-integrated JWST NIRSpec time series photometry of WASP-107 b is shown in Fig. 1 and the transmission spectrum is shown in Fig. 2. The spectrum shows several molecular
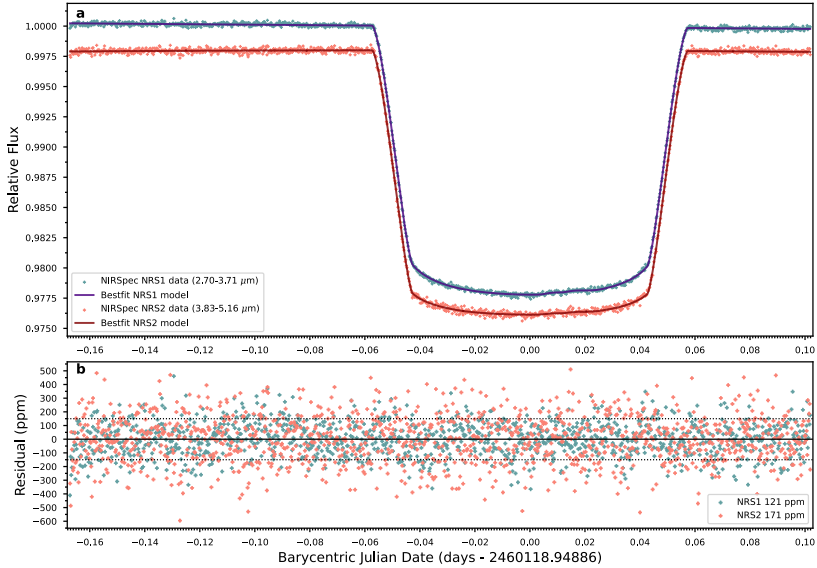
Fig. 1 The light curve of WASP-107b observed by JWST NIRSpec G395H. (**a**) The normalized wavelength-integrated white light curves for the two detectors are shown, with the NRS1 (2.7-3.71 μm) and NRS2 (3.83-5.16 μm) detectors offset for clarity. A best-fit limb-darkenened transit model is overplotted (blue). See Extended Data Fig. 2 for additional details. (**b**) The model residuals which achieve near-photon limited precisions.

absorption signals that are readily identifiable. We detect a large CO_2 absorption feature at 4.3 μm[19] (see Fig. 2) and a slope-like feature at the shortest wavelengths from H_2O[18].

We ran a series of model retrievals to provide detailed constraints on the atmospheric composition and temperature (Methods). The H_2O and CO_2 features are detected at high confidence (see Extended Data Table 2). The spectrum shows CO features between 4.5 and 5 μm (4σ), and an SO_2 absorption feature at 4.0 μm (5.5σ). SO_2 is a known by product of photochemistry[7], being generated when stellar UV radiation reacts with H_2S, and has been identified in WASP-107 b at longer wavelengths with JWST/MIRI[4]. Finally, a narrow CH_4 feature is identified at 3.32μm (4.2σ). While CH_4 has been unobservable at both shorter and longer wavelengths[2, 4] the feature here is the Q-branch band head of CH_4 which is strong enough to appear above the clouds and H_2O (see Fig. 2).

For H_2O, we find volume mixing ratio abundances of $10^{-1.85\pm0.22}$ which indicates super-solar abundances near 40× solar. The presence of CO_2 is known to be a tracer of high metallicity[19, 21], and the retrieved abundances of $10^{-3.33\pm0.27}$ support this, though are lower than chemical equilibrium expectations by about an order of magnitude as the molecule is further sensitive to atmospheric mixing. CH_4 is also found to be heavily depleted, with retrieved abundances of $10^{-6.03\pm0.21}$. These CH_4 abundances are consistent with previous HST and JWST upper limits[2, 4]. At the millibar pressures probed in transmission spectra, at 40× solar the atmosphere in equilibrium would be about one part in a thousand CH_4, while abundances slightly less than one part per million (ppm) are found. Measuring the amount of CH_4 depletion is highly constraining for non-equilibrium models[8], as it can be tied to the pressure and temperature of the hotter interior from which the species is mixed to higher levels. While not every planet is showing a CH_4 depletion[5], for those that do
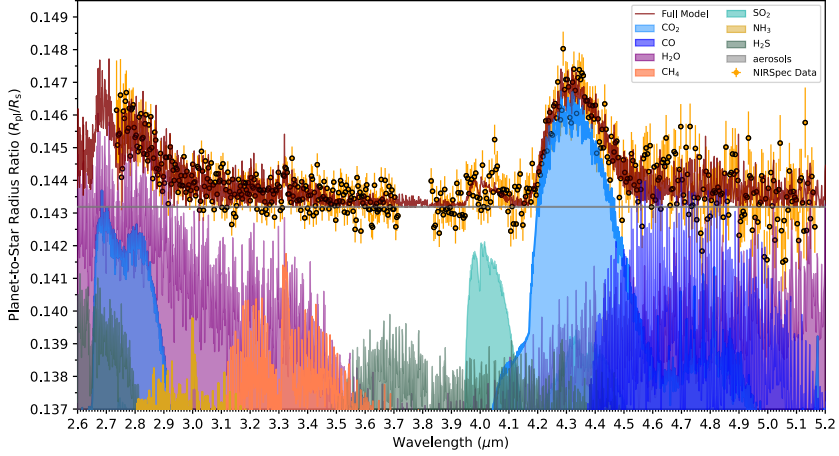
Fig. 2 WASP-107 b transmission spectral measurements. Shown is the JWST NIRSpec transmission spectrum and the 1-σ uncertainties. The best-fit ATMO[20] model is also plotted, as well as the individual contributions for each molecular species.

such as WASP-107 b[4] and others[3], only upper-limits on the depletion have been available. By quantifying the CH_4 depletion, the non-equilibrium chemistry can be tightly constrained and the depletion mechanisms can be explored. We find abundances of SO_2 to be $10^{-5.06\pm0.13}$ which broadly match the JWST/MIRI results[4] as well as those of WASP-39 b[7, 22] indicating ongoing photochemistry in the atmosphere.

Given the retrieved molecular abundances, we ran a grid of forward atmospheric models to place constraints on the photochemistry, vertical mixing, metallicity and temperature structure of the planet. The model and includes non-equilibrium chemistry from both vertical mixing and photochemistry self consistently calculated[23,24] (Methods). The chemistry was computed using temperature-pressure profiles in radiative-convective equilibrium, with a range of intrinsic temperatures, T_{int}. The intrinsic temperature is related to the emitted flux generated from the planet's interior which passes through the atmosphere, with Jupiter having a T_{int} near 100 K. With vertical mixing, the major molecular species detected are expected to be uniformly mixed from their quench pressures at deeper/hotter conditions in chemical equilibrium to higher altitudes. We modeled

the vertical mixing in a turbulent flow using the vertical eddy diffusion coefficient, K_{zz}. Our best-fit forward model to the retrieved abundances are shown in Fig. 3 (see also Extended Data Fig. 7).

We find the combination of H_2O, CO, CO_2, CH_4 and SO_2 to be highly constraining. H_2O and CO are insensitive to non-equilibrium chemistry in this temperature regime (see Fig. 3) helping to uniquely measure the metallicity while the combination of CO_2 and CH_4 are jointly sensitive to K_{zz} and T_{int}. SO_2 also helps provide an upper bound on K_{zz} (see Extended Data Fig. 7). With these combined constraints, the forward model grid indicates the planet has a hot intrinsic temperature of T_{int} =460±40 K, a high metallicity of Z=43±8× solar and vigorous vertical mixing with a K_{zz}= $10^{11.6\pm0.1}$ cm^2/s.

Theoretical models have estimated the strength of vertical mixing and K_{zz}[13,14,15]. However, the overall uncertainty on K_{zz} for giant planets remains large[16], with values often ranging from 10^4 to 10^{12} cm^2/s in the context of hot Jupiters[8]. The empirical constraints on K_{zz} for exoplanets currently rely on broadband Spitzer/IRAC photometry[9], where there is considerable planet-to-planet stochasticity and the molecular features are spectroscopically unresolved which gives rise to modeling
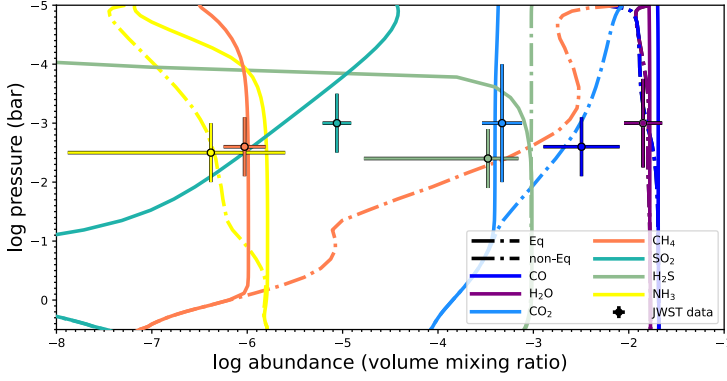
Fig. 3 Model Interpretation Figure. ATMO non-equilibrium chemistry model with vertical mixing and photochemistry. The best-fit non-equilibrium chemistry model is shown (solid lines) as well as the abundance profiles in equilibrium (dot-dashed lines). The retrieved JWST abundances are shown (data points) with the model grid indicating the planet has hot interior temperatures (T_{int}=458±38 K), a super-solar metallicity (Z/Z$_\odot$=43±8) with vigorous vertical mixing (K_{zz} = $10^{11.6±0.1}$ cm^2/s).

degeneracies. The K_{zz} measurement in WASP-107 b here is a substantial improvement over the order of magnitude estimates previously explored using either the upper limits on CH$_4$ from JWST/MIRI[4] or population-level results[9]. The measurement is best evidence to-date that non-equilibrium chemistry from vertical mixing is an important physical process in exoplanetary atmospheres, a mechanism long known to be important for Jupiter[25]. The K_{zz} value for WASP-107 b at 1 bar is about 1,000 to 10,000× higher than the typical estimates used[7,26] which are largely based on 3D GCM modeling[13]. This could indicate the planet has anomalously high vertical mixing, perhaps due to the high T_{int} resulting in a convective region which reaches lower than expected pressures. Alternatively, the GCM models may be inadequately capturing the eddy dissipation with the artificial viscosity parameters used[27].

The high T_{int} is a direct constraint on the energy stored in the deep atmosphere, which can help us understand the mechanism responsible for the inflated radius of the planet. The anomalously large radii of irradiated warm Neptunes/hot Jupiters are one of the most intriguing and long-standing problems in our understanding of extrasolar giant planets with several proposed mechanisms including: tidal heating[28],

downward transport of kinetic energy[29], enhanced opacities[30], ongoing layered convection[31], ohmic dissipation[32], and more recently the advection of potential temperature[20, 33]. The potential temperature mechanism has been recently demonstrated in the hot Jupiter WASP-76b using first principle radiative GCM simulations[34]. The hot interior temperature can explain the higher vertical mixing rates found, as hotter temperatures and lower surface gravities are expected to both increase K_{zz}. These high vertical mixing rates with supersolar metallicities and hot intrinsic temperatures in turn also explain the cloud properties observed, where silicate cloud particles were surprisingly found with JWST/MIRI[4]. For planets like WASP-107 b with equilibrium temperatures near 770 K, the condensation of silicate clouds should be occurring at high unobservable pressures if T_{int} was low (∼100 K)[8]. However, with a high T_{int} of 460 K the silicate cloud base is moved to ∼bar pressures (see Extended Data Fig. 6) and the high K_{zz} values found here are more than sufficient to aloft the cloud particles to mbar pressures where they are observed in transmission.

The mass, radius, and T_{int} alone constrain the overall bulk metallicity of the planet to be Z_p= 63.5$^{+10.4}_{-8.5}$ %. A precise atmospheric metallicity and T_{int} allows us to place better

constraints on the planet's overall metal content and estimate the planet's core mass (Methods). To date, no gas giant exoplanet has had the presence of a core significantly detected, with upper limits reported for HAT-P-13 b[35] and WASP-107 b[10]. Any metals seen in the bulk but not in the atmosphere must be hidden in the interior in a core or composition layers. Assuming a uniform composition core, an isothermal 50-50% mixture of rock and water, gives us $M_c = 11.5^{+3.0}_{-3.6} \ M_\oplus$ – which is a third the mass of the planet and the first statistically-significant core detection for a giant exoplanet. This value is much higher than previous estimates limiting the core to < 4.6 $M_\oplus$[10], which had assumed the planet followed a standard cooling track with no tidal heating. These low core-mass values were in tension with standard core-accretion models[11] which do not predict such a light core could accrete the massive H/He envelope observed. In contrast, our core mass estimate matches the $\sim 10 \ M_\oplus$ prediction needed to elicit runaway gas accretion within the disks lifetime. It's worth noting that the structure of the interior may not be exactly an envelope-on-core model, but may be more like Neptune and Uranus with a rocky core and an icy water mantle[36] or the core may be diffuse and/or similar to Jupiter[37, 38]. The core mass result should be understood as the total excess non-H/He heavy elements in the interior, irrespective of exactly how it is structured. With the proof-of-concept demonstrated here, using CH_4-depletion as a thermometer of the deep atmosphere for other gas giant exoplanets could help provide constraints at the population level about how planetary cores might differ with planet or host star mass and metallicities.

WASP-107 b is one of the lowest density planets known, which has led to speculation that the planet have formed substantially different than the solar system, with dust-free accretion or in-situ scenarios explored[10]. However, the important bulk properties found here line up well with the solar-system (SS) planets indicating a similar core-accretion scenario. In particular, with a metallicity of 43±8× solar, WASP-107 b is close to the mass-metallicity trend of the gas giant SS planets[39]. In addition, with an estimated core mass of $11.5^{+3.0}_{-3.6} \ M_\oplus$, WASP-107 b is also intermediate between Neptune and Saturn, falling reasonably along their lines of formation[40,41]. The major difference for WASP-107 b appears to be its much hotter interior, resulting in an extremely puffy planet.

References

[1] Stevenson, K. B. *et al.* Possible thermochemical disequilibrium in the atmosphere of the exoplanet GJ 436b. *Nature* **464**, 1161–1164 (2010).

[2] Kreidberg, L., Line, M. R., Thorngren, D., Morley, C. V. & Stevenson, K. B. Water, High-altitude Condensates, and Possible Methane Depletion in the Atmosphere of the Warm Super-Neptune WASP-107b. *Astrophys. J. L.* **858**, L6 (2018).

[3] Fu, G. *et al.* Water and an Escaping Helium Tail Detected in the Hazy and Methane-depleted Atmosphere of HAT-P-18b from JWST NIRISS/SOSS. *Astrophys. J. L.* **940**, L35 (2022).

[4] Dyrek, A. *et al.* SO_2, silicate clouds, but no CH_4 detected in a warm Neptune. *Nature* **625**, 51–54 (2024).

[5] Bell, T. J. *et al.* Methane throughout the atmosphere of the warm exoplanet WASP-80b. *Nature* **623**, 709–712 (2023).

[6] Madhusudhan, N. *et al.* Carbon-bearing Molecules in a Possible Hycean Atmosphere. *Astrophys. J. L.* **956**, L13 (2023).

[7] Tsai, S.-M. *et al.* Photochemically produced SO_2 in the atmosphere of WASP-39b. *Nature* **617**, 483–487 (2023).

[8] Fortney, J. J. *et al.* Beyond Equilibrium Temperature: How the Atmosphere/Interior Connection Affects the Onset of Methane, Ammonia, and Clouds in Warm Transiting Giant Planets. *Astron. J.* **160**, 288 (2020).

[9] Baxter, C. *et al.* Evidence for disequilibrium chemistry from vertical mixing in hot Jupiter atmospheres. A comprehensive survey of transiting close-in gas giant exoplanets with warm-Spitzer/IRAC. *Astron. Astrophys.* **648**, A127 (2021).

[10] Piaulet, C. *et al.* WASP-107b's Density Is Even Lower: A Case Study for the Physics of Planetary Gas Envelope Accretion and Orbital Migration. *Astron. J.* **161**, 70 (2021).

[11] Pollack, J. B. *et al.* Formation of the Giant Planets by Concurrent Accretion of Solids and Gas. *Icarus* **124**, 62–85 (1996).

[12] Anderson, D. R. *et al.* The discoveries of WASP-91b, WASP-105b and WASP-107b: Two warm Jupiters and a planet in the transition region between ice giants and gas giants. *Astron. Astrophys.* **604**, A110 (2017).

[13] Parmentier, V., Showman, A. P. & Lian, Y. 3D mixing in hot Jupiters atmospheres. I. Application to the day/night cold trap in HD 209458b. *Astron. Astrophys.* **558**, A91 (2013).

[14] Zhang, X. & Showman, A. P. Global-mean Vertical Tracer Mixing in Planetary Atmospheres. I. Theory and Fast-rotating Planets. *Astrophys. J.* **866**, 1 (2018).

[15] Menou, K. Turbulent vertical mixing in hot exoplanet atmospheres. *Mon. Not. R. Astron. Soc.* **485**, L98–L103 (2019).

[16] Mukherjee, S. *et al.* Probing the Extent of Vertical Mixing in Brown Dwarf Atmospheres with Disequilibrium Chemistry. *Astrophys. J.* **938**, 107 (2022).

[17] Birkmann, S. M. *et al.* The Near-Infrared Spectrograph (NIRSpec) on the James Webb Space Telescope IV. Capabilities and predicted performance for exoplanet characterization. *Astron. Astrophys.* **661**, A83 (2022).

[18] Alderson, L. *et al.* Early Release Science of the exoplanet WASP-39b with JWST NIRSpec G395H. *Nature* **614**, 664–669 (2023).

[19] The JWST Transiting Exoplanet Community Early Release Science Team *et al.* Identification of carbon dioxide in an exoplanet atmosphere. *Nature* **614**, 649-652 (2023).

[20] Tremblin, P. *et al.* Advection of Potential Temperature in the Atmosphere of Irradiated Exoplanets: A Robust Mechanism to Explain Radius Inflation. *Astrophys. J.* **841**, 30 (2017).

[21] Moses, J. I., Madhusudhan, N., Visscher, C. & Freedman, R. S. Chemical Consequences of the C/O Ratio on Hot Jupiters: Examples from WASP12b, CoRoT-2b, XO-1b, and HD 189733b. *Astrophys. J.* **763**, 25 (2013).

[22] Rustamkulov, Z. *et al.* Early Release Science of the exoplanet WASP-39b with JWST NIRSpec PRISM. *Nature* **614**, 659–663 (2023).

[23] Drummond, B. *et al.* The effects of consistent chemical kinetics calculations on the pressure-temperature profiles and emission spectra of hot Jupiters. *Astron. Astrophys.* **594**, A69 (2016).

[24] Nicholls, H., H´ebrard, E., Venot, O., Drummond, B. & Evans, E. Temperature-chemistry coupling in the evolution of gas giant atmospheres driven by stellar flares. *Mon. Not. R. Astron. Soc.* **523**, 5681–5702 (2023).

[25] Prinn, R. G. & Barshay, S. S. Carbon Monoxide on Jupiter and Implications for Atmospheric Convection. *Science* **198**, 1031–1034 (1977).

[26] Moses, J. I., Tremblin, P., Venot, O. & Miguel, Y. Chemical variation with altitude and longitude on exo-Neptunes: Predictions for Ariel phase-curve observations. *Experimental Astronomy* **53**, 279–322 (2022).

[27] Mayne, N. J. *et al.* The unified model, a fully-compressible, nonhydrostatic, deep atmosphere global circulation model, applied to hot Jupiters. ENDGame for a HD 209458b test case. *Astron. Astrophys.* **561**, A1 (2014).

[28] Bodenheimer, P., Lin, D. N. C. & Mardling, R. A. On the Tidal Inflation of Short-Period Extrasolar Planets. *Astrophys. J.* **548**, 466–472 (2001).

[29] Showman, A. P. & Guillot, T. Atmospheric circulation and tides of "51 Pegasus b-like" planets. *Astron. Astrophys.* **385**, 166–180 (2002).

[30] Burrows, A., Hubeny, I., Budaj, J. & Hubbard, W. B. Possible Solutions to the Radius Anomalies of Transiting Giant Planets. *Astrophys. J.* **661**, 502–514 (2007).

[31] Chabrier, G. & Baraffe, I. Heat Transport in Giant (Exo)planets: A New Perspective. *Astrophys. J. L.* **661**, L81–L84 (2007).

[32] Batygin, K., Stevenson, D. J. & Bodenheimer, P. H. Evolution of Ohmically Heated Hot Jupiters. *Astrophys. J.* **738**, 1 (2011).

[33] Sainsbury-Martinez, F. *et al.* Idealised simulations of the deep atmosphere of hot Jupiters. Deep, hot adiabats as a robust solution to the radius inflation problem. *Astron. Astrophys.* **632**, A114 (2019).

[34] Sainsbury-Martinez, F. *et al.* Evidence of radius inflation in radiative GCM models of WASP-76b due to the advection of potential temperature. *Mon. Not. R. Astron. Soc.* **524**, 1316–1325 (2023).

[35] Buhler, P. B. *et al.* Dynamical Constraints on the Core Mass of Hot Jupiter HAT-P-13b. *Astrophys. J.* **821**, 26 (2016).

[36] Cavalié, T. *et al.* The Deep Composition of Uranus and Neptune from In Situ Exploration and Thermochemical Modeling. *Space Sci. Rev.* **216**, 58 (2020).

[37] Vazan, A., Helled, R. & Guillot, T. Jupiter's evolution with primordial composition gradients. *Astron. Astrophys.* **610**, L14 (2018).

[38] Debras, F. & Chabrier, G. New Models of Jupiter in the Context of Juno and Galileo. *Astrophys. J.* **872**, 100 (2019).

[39] Thorngren, D. P., Fortney, J. J., Murray-Clay, R. A. & Lopez, E. D. The Mass-Metallicity Relation for Giant Planets. *Astrophys. J.* **831**, 64 (2016).

[40] Guillot, T. *et al.* Giant Planets from the Inside-Out. *arXiv e-prints* arXiv:2205.04100 (2022).

[41] Mankovich, C. R. & Fuller, J. A diffuse core in Saturn revealed by ring seismology. *Nature Astronomy* **5**, 1103–1109 (2021).
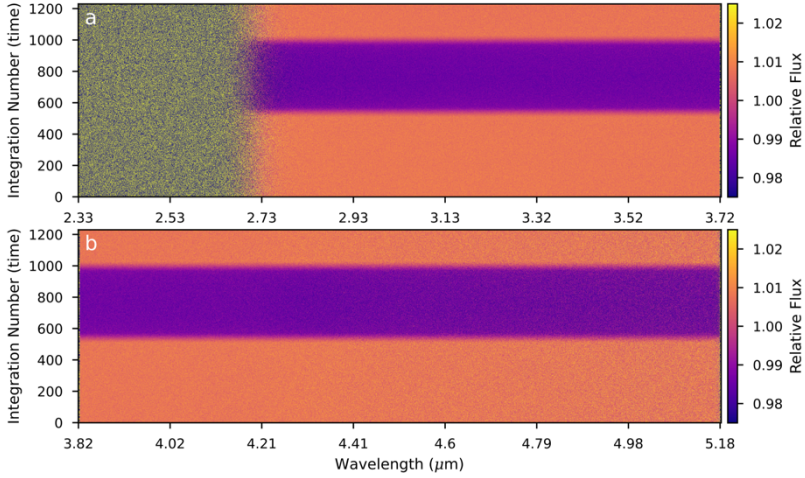
Extended Data Figure 1 FIREFLy transit light curve spectrophotometry. Shown is the relative flux as a function of wavelength and time for NIRSpec detectors (**a**) NRS1 and (**b**) NRS2.

Parameter	Value	Description	Reference
P	5.7214742 ± 0.0000043		[45]
T_0	$2460118.948861 \pm 0.0000063$	Mid-transit time days (BJD$_{\mathrm{TDB}}$)	this work
$a/R_\star$	18.0923 ± 0.0212	Scaled semi-major axis	this work
b	0.11650 ± 0.01199	Transit impact parameter	this work

Extended Data Table 1 Orbital parameters. Best-fit orbital parameters as measured from the FIREFLy JWST white light curve.

Methods

Data Reduction

One transit of WASP-107 b was observed on 2023 June 23 with JWST for 6.5 hours using the NIRSpec instrument with the G395H grating. This setup gives a wavelength range from 2.7 to 5.18 μm with the corresponding resolving power ranging between 1828 to 3600. The instrument used the NRSRAPID readout pattern and SUB2048 subarray with 20 groups per integration, resulting in 1230 integrations over the 6.5 hour observation.

FIREFLy

We reduce the data using the Fast InfraRed Exoplanet Fitting Lyghtcurve (FIREFLy)[22, 42] reduction suite, which starts with a customized reduction using the STScI pipeline and the uncalibrated images. Our custom reduction includes $1/f$ destriping at the group level before the ramp is fit. The jump-step and dark-current stages of the STScI pipeline were skipped. We then use the custom-run pipeline 2D images after the gain

scale step, and perform customized cleaning of bad pixels, cosmic rays and hot pixels. Using cross-correlation, we measured the positional shift of the spectral trace across the detector and shift-stabilized the images with flux-conserving interpolation. This procedure has been found to reduce the amplitude of position-dependent trends[22, 42], as the underlying stellar spectra is not shifting in wavelength across a pixel through the time series. We note nearly identical results can be found if the data is not shift-stabilized and the extraction window is moved instead. Further position-dependent trends can be expected from intrapixel sensitivity variations[17], though their magnitude on-sky has been very small as JWST generally has excellent pointing with the detector shifts found in this dataset to be on the order of ~1/1000 of a pixel. We optimized the width of our flux extraction aperture to minimize the standard deviation of the white light curve photometry and extracted the spectrophotometric time series. The 2D extracted spectral time series can be seen in Extended Data Fig. 1. We extracted the
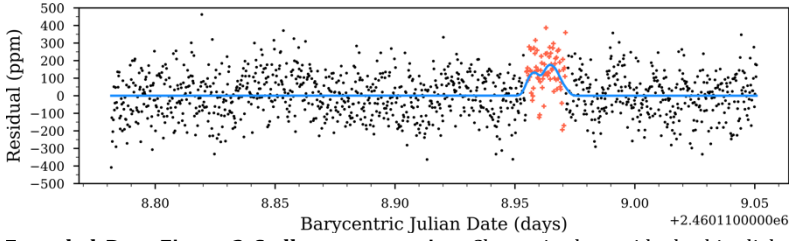
Extended Data Figure 2 Stellar spot-crossing. Shown is the residual white-light curve photometry from NRS1 when fitting for the non-spotted data (black dots). The suspected occulted spot (red crosses) is shown, with a Gaussian smoothed filter overplotted (blue line).

transmission spectra with a range of different wavelength bin sizes, reporting an extraction with a resolution near R=950.

We fit the transit light curves using a quadratic function to model stellar limb darkening given as,

$$\frac{I(\mu)}{I(1)} = 1 - a(1 - \mu) - b(1 - \mu)^2 . \quad (1)$$

where $I(1)$ is the intensity at the center of the stellar disk, $\mu = cos(\theta)$ where θ is the angle between the line of sight and the emergent intensity, and a and b are the limb darkening coefficients. In practice, we remap a and b and fit instead for q_1 and q_2 which has shown to be less degenerate[43]. The resulting limb-darkening coefficients can be seen in Extended Data Fig. 3.

Model limb darkening coefficients calculated from 3D models[44] capture the wavelength dependence of limb-darkening well, but we find an overall offset in the coefficients of -0.0378 and +0.175 for q_1 and q_2 respectively. We applied these offsets to the wavelength dependent model limb-darkening

coefficients and re-fit the transmission spectra with fixed limb-darkening. This iterative procedure reduces the bin-to-bin scatter of the transmission spectra as the limb-darkening is fixed, but allows for overall differences between the transit data and stellar model limb-darkening. We bin the spectrophotometry into 576 wavelength bins, providing a spectral resolution of R~950 for the planet.

Stellar Spot Crossing

A stellar spot crossing event is observed in our transit light curve data, appearing in both NRS1 and NRS2 shortly after mid-transit, which we decontaminated from the light curves and the transmission spectrum. The host star is known to be modestly active[12], with optical photometric modulations of ~0.4% on a period of about 17 days. We modeled this spot empirically, first fitting the non-spotted region with a transit light curve and using the overall residual in the spotted region to define the photometric shape of the spot (see Extended Data Fig. 2.) A Gaussian filter was then applied to the spot-shape and
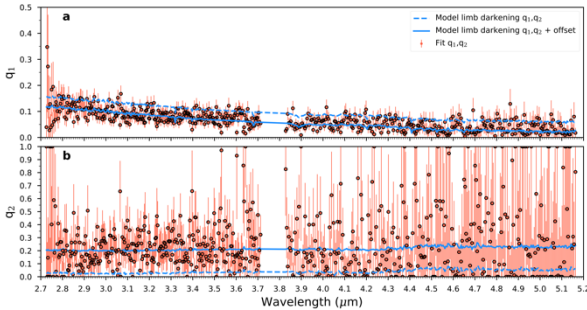
Extended Data Figure 3 Limb-Darkening. Shown are the resulting stellar limbdarkening coefficients q_1 (**a**) and q_2 (**b**) derived from the transit light curves using a quadratic law. The limb-darkening coefficients derived from a stellar model are also shown, along with the models with an offset derived from the difference between the data and model.

subsequently used to model the full transit light curves, fitting for a scaling factor. As the spot is low in amplitude and only covers a small portion of the data, our overall transmission spectrum is insensitive to the occulted spot. We found equivalent results between masking the region for all the transit light curve fits and fitting for the spot shape in the light curves.

TEATRO

An independent data reduction was performed using the Transiting Exoplanet Atmosphere Tool for Reduction of Observations (TEATRO) pipeline.
The data were processed using the jwst calibration software package version 1.10.2, CRDS version 11.16.19, CRDS context 1147[115, 116], starting from the 'uncal' files. For stage 1, a jump rejection threshold of 6 was used and the 'jump.flag 4 neighbors' parameter was turned off. For stage 2, the flat field and photometric calibration steps were skipped. Bad pixels and missing pixels were then corrected for in each integration. The center of the spectral trace in the spatial direction was computed by fitting a Gaussian function to each column and fitting a third order polynomial to their maxima. For each integration, the background was computed on a column-by-column basis using pixels above and below the spectral trace (or only one of them at the short and long wavelength edges of NRS2).

An aperture half-width of 2.73 and 3 pixels and background regions starting 6.5 and 6 pixels further away were used for nrs1 and nrs2, respectively. The background subtraction and spectral extraction were performed using the 'extract 1d' routine with the corresponding polynomial coefficients as parameters. The whitelight flux was computed using the 'white light' step routine. For the spectroscopic analysis, we binned the spectra in 86 and 136 wavelength bins of 0.01 μm width, covering the 2.86 – 3.72μm and 3.82–5.18μm ranges with nrs1 and nrs2, respectively. The lightcurves were normalized

by the out of transit flux and a 5-iteration 3.5 sigma-clipping was applied to remove outliers.

Lightcurve fits were performed using the exoplanet[117, 118] package with a quadratically limb darkened transit lightcurve model and a second order polynomial to account for long term trends. A fit to the whitelight curve obtained from NRS1 only was first performed to derive system parameters (mid-transit time, impact parameter, planet to star radius ratio, stellar density). These parameters were then fixed for the spectroscopic lightcurve fits, leaving only the radius ratio and polynomial trend as free parameters. Limb-darkening coefficients were obtained from ExoTETHyS[119], they were free for the whitelight curve fit and fixed for the spectroscopic lightcurve fits. The median of the posterior distribution of the radius ratio was used to derive the transit depth in each wavelength bin. The uncertainties were computed by summing quadratically the standard deviations of the in- and -out-of-transit parts of the lightcurve divided by the square root of their respective number of points (this gave a better estimate than the standard deviation of the posterior distributions).

Comparing the TEATRO reduction to FIREFLy, we find good consistency with the spectra agreeing at the point-to-point level at better than 1-σ for both NRS1 and NRS2.

Resolution-linked Bias

We have adjusted the retrieved abundance to account for the resolution-linked bias (RLB) effect[46], in which planetary absorption signatures are diluted within stellar absorption lines. For G395H data, this in particular dilutes the transmission spectral signatures of CO, as the molecule is found in both the star and planet's atmosphere. We followed the method in Ref. [42], estimating the magnitude of the effect using high-resolution models. Compared to WASP-39A, WASP-107A is a cooler later-type star which enhances the RLB effect as the stellar CO is

stronger. However, within the CO lines, the planet's atmosphere is cloudier than WASP-39b, which somewhat reduces the effect. In total, we find the RLB reduces the inferred CO abundance by 0.2 dex, which is about half of the uncertainty in the CO abundance.

Atmospheric Models
ATMO Setup

We use ATMO, a 1D-2D radiative-convective equilibrium model for planetary atmospheres to generate models of WASP-107 b. More comprehensive descriptions of the model can be found in Refs. [20, 47,48,49,50], and [51]. The ATMO model is used here as both a forward physical model in radiative and chemical (dis-)equilibrium and a retrieval model where the abundances and temperature-pressure profile are let free to fit the data. By comparing the retrieved and forward model abundances within a single model suite, model-to-model systematics from such sources as differences in opacites can be avoided. ATMO has been validated against the publicly available MET office radiative transfer code SOCRATES[52], and has been benchmarked against Exo-REM[53] and petitCODE[54] in the context of JWST observations[55].

ATMO solves the radiative transfer equation with isotropic scattering in 1D plane-parallel geometry for the irradiation and thermal emission, finding a pressure-temperature (P-T) profile that satisfies hydrostatic equilibrium and conservation of energy and is also self-consistent with the atmospheric chemistry and opacities, given a set of elemental abundances. The total opacity of the gas mixture is computed using the correlated-k approximation using the random overlap method with resorting and rebinning[47, 56]. The k-coefficients are calculated 'on the fly' for each atmospheric layer, spectral band and iteration such that the derived opacities are physically self-consistent with the T-P profile and chemical composition. ATMO can be also used as a full line-by line code at high spectral resolution,

though that is not used here as it is too computationally heavy for spectral retrieval purposes. The spectrally active species currently include H_2-H_2 and H_2He collision induced absorption (CIA) opacities, as well as H_2O, CO_2, CO, CH_4, NH_3, Na, K, Li, Rb, Cs, TiO, VO, Fe, FeH, CrH, PH_3, HCN, C_2H_2, H_2S, SO_2 and H- (see Refs. [57, 58] full description). Multi-gas Rayleigh scattering contributions from the different species are also included.

The chemical abundances in equilibrium are determined by minimizing the Gibbs free energy following the method of Ref.[59], and using the thermochemical data from Ref. [60]. Solar elemental abundances are set from Refs. [61, 62], with the chemistry fully flexible for any mix of input elemental abundances. This method also allows for the depletion of gas phase species due to condensation as well as thermal ionization and dissociation. ATMO has as several different chemical schemes which can be chosen, and by default calculates the abundances for 175 neutral, 9 ionic, and 93 condensate species. Condensation can be treated locally, or with rainout. Rainout is treated by calculating the chemistry at the highest pressure initially, then following the T-P profile towards lower pressures. Condensed elements are removed locally, as well as for all lower pressures[63], allowing for opacity changes which can alter the radiative-convective balance and P-T profile.

For non-equilibrium C-H-N-O chemistry, ATMO uses a chemical kinetics scheme from Ref. [64] as described in Ref. [50]. As done in Ref. [7] to model the S photochemistry of WASP-39 b with ATMO, we used the thermochemical network from Ref. [65] along with the photochemical scheme from Ref. [66] including 71 photolysis reactions of H_2S, S_2, SO_2, SO, SO_2, CH_3SH, SH, H_2SO and COS.
ATMO includes a relatively simple treatment of clouds and hazes [57] and does not consider the distribution of aerosol particles. An aerosol 'haze' scattering is implemented as enhanced Rayleigh-like scattering [67], presented as

$$\sigma(\lambda)_{haze} = \delta_{haze}\, \sigma_0 (\lambda/\lambda 0)^{-\alpha_{haze}}, \qquad (2)$$

Parameter	Value & 1-σ Uncertainty	Detection (σ)	Value & 1-σ Uncertainty
	ATMO Retrieval		NEMESIS Retrieval
Atmosphere Temperature (K)	482^{+14}_{-13}		474^{+17}_{-11}
R_{pl} (R_J)	$0.9477^{+0.0013}_{-0.0015}$ (mbar)		0.88 ± 0.01 (100 bar)
cloud δ_{cloud}	$1.91^{+0.20}_{-0.14}$		
log (cloud top) (bar)			$-3.74^{+0.12}_{-0.16}$
VMR log(H_2O)	$-1.85^{+0.22}_{-0.23}$	17	$-1.72^{+0.26}_{-0.16}$
VMR log(CO)	$-2.70^{+0.28}_{-0.48}$	4	$-3.85^{+0.62}_{-0.87}$
VMR log(CO_2)	$-3.33^{+0.25}_{-0.25}$	43	$-2.62^{+0.36}_{-0.34}$
VMR log(CH_4)	$-6.03^{+0.22}_{-0.20}$	4.2	$-6.14^{+0.42}_{-1.70}$
VMR log(SO_2)	$-5.06^{+0.14}_{-0.15}$	5.5	$-4.59^{+0.19}_{-0.18}$
VMR log(H_2S)	$-3.48^{+0.32}_{-1.35}$	2.0	$-7.10^{+3.18}_{-3.00}$
VMR log(NH_3)	$-6.38^{+0.78}_{-1.54}$	1.5	$-8.12^{+1.99}_{-2.36}$
VMR log(HCN)			$-9.12^{+2.01}_{-1.94}$
	ATMO Non-Equilibrium Forward		
Metallicity, $Z/Z_\odot$	43 ± 8		
Intrinsic Temperature, T_{int} (K)	458 ± 38		
Diffusion coeff., $\log[K_{zz}$ (cm^2/s)]	11.6 ± 0.1		

Extended Data Table 2 Model Results. The retrieval results from the ATMO and NEMESIS codes are given, with the best-fit parameter values shown along with their 1-σ uncertainties. T_{int} refers to the intrinsic temperature, which is related to the flux, F, emitted from the planet's interior by $F=\sigma_R T_{int}^4$, where σ_R the Stefan-Boltzmann constant. VMR refers to the Volume Mixing Ratio.

where $\sigma(\lambda)$ is the total scattering cross-section of the material, δ_{haze} is an empirical enhancement factor, and σ_0 is the scattering cross section of molecular hydrogen at 0.35 μm, and α_{haze} is a factor determining the wavelength dependence with α_{haze} = 4 corresponding to Rayleigh scattering. Condensate 'cloud' absorption is assumed to have a grey wavelength dependence, and is calculated as

$$\kappa(\lambda)_{cloud} = \delta_{cloud}\,\kappa_{H2}, \qquad (3)$$

where $\kappa(\lambda)_{cloud}$ is the 'cloud' absorption opacity, δ_{cloud} is an empirical factor governing the strength of the grey scattering, and κ_{H2} is the scattering opacity due to H_2 at 0.35 μm. $\sigma(\lambda)_{haze}$ and $\kappa(\lambda)_{cloud}$ are added to the total gaseous scattering and absorption respectively.

For spectra retrievals, we coupled the forward ATMO model to a nested sampling statistical algorithm to marginalize the posterior distribution and measure the model evidence [68,69,70]. The retrieval aspects of ATMO were developed to fit transit and eclipse data, with results published for a number of transiting planets (e.g. Refs [3, 71, 72, 73, 74, 75]). A main difference compared to the forward models is the retrieval does not converge the TP profile to radiative-convective equilibrium, but rather parameterizes the profile which is then fit against the planetary spectrum. With the retrieval model, the k-coefficients are still calculated 'on the fly' in the same way as described in the forward model (and

equilibrium chemistry if specified) for every likelihood evaluation step to maximize accuracy and consistency. To parameterize the T-P profile, we use the three channel (two optical, one infrared) analytic radiative equilibrium model as described in Ref. [76], which is based on the derivations by Ref. [77].

ATMO WASP-107b Retrievals

For the NIRSpec WASP-107 b data, we found the flexible parameterized P-T profile simply fit to a simple isotherm, so we instead fit for a single isothermal temperature for the atmosphere. Given the planet's atmosphere is far out of equilibrium, we fit a constant VMR for each molecule. In addition to the cloud, we included the spectrally active species of H_2H_2, H_2-He (CIA) opacities, H_2O[78], CO_2[79], CO[80], CH_4[81], NH_3[82], H_2S[83], and SO_2[84].

We searched the G395H data for H_2S, and can marginally improve the model fits to the data, but its inclusion is not supported with confidence by the Bayesian evidence. Considerable opacity from aerosols are also needed to fit the spectrum, which is in-line with previous *HST* results where H_2O and He features are observed between 0.9 and 1.6 μm peaking above the clouds[2, 73]. We fit the data with a grey cloud and a scattering haze, but found only a grey cloud was needed to fit the data (see Extended Data Table 3). In addition, we found the choice of cloud parameterization did not have a strong influence on the retrieved abundances. Fitting the grey cloud with either a single uniform opacity or for a cloud-top pressure also gave similar results. A

aerosol model	parameters	model selection	VMR CH$_4$	log[K_{zz} (cm^2/s)]
	ATMO Retrieval	ΔBIC		
grey cloud	δ_{cloud}	-	$-6.03^{+0.22}_{-0.20}$	11.60 ± 0.11
cloud + haze	$\delta_{cloud}, \delta_{haze}, \alpha_{haze}$	5.0	$-6.29^{+0.19}_{-0.26}$	11.56 ± 0.09
grey cloud	log(cloud top)	5.3	$-5.96^{+0.24}_{-0.25}$	11.47 ± 0.11
	NEMESIS Retrieval	Δ(lnBE)		
grey cloud	log(cloud top)	-	$-6.14^{+0.42}_{-1.70}$	
grey cloud	δ_{cloud}	-4.1	$-5.86^{+0.35}_{-0.85}$	
enstatite cloud	δ_{cloud}	-20.0	$-5.38^{+0.23}_{-0.27}$	

Extended Data Table 3 Aerosol Cloud Retrieval Comparisons. BIC refers to the Bayesian information criterion, while BE refers to the Bayesian Evidence. Both statistics are calculated relative to the best-fit model given a value of '-'.

narrow feature of NH$_3$ is potentially found in the data at 3.0 microns, but similar to H$_2$S, its identification is not supported with high confidence by the Bayesian evidence. NH$_3$ has been marginally detected at longer wavelengths with JWST/MIRI, indicating the molecule could be confidently identified with a dedicated multi-wavelength study.

The retrieval constraints are given in Extended Data Table 2. CO is found to have abundances of $10^{-2.7\pm0.4}$, which is slightly low relative to 40× solar values derived from H$_2$O. While low, the uncertainty on the CO abundance is large as the feature is subtle in the data and H$_2$O and clouds help mask the signature. A confounding factor regarding CO is a resolution-linked-bias (RLB) effect[22, 46], where CO present in the stellar spectra dilutes the strong molecular line cores in the planetary transmission spectrum. This does not affect H$_2$O, CH$_4$ or CO$_2$ as those molecules

Extended Data Figure 4 WASP-107 b retrieval posteriors. Shown is the distribution for the ATMO free-retrieval. VMR refers to the Volume Mixing Ratio of the molecular species. 1, 1.5, and 2-σ equivalent contours are shown. The 1D histograms show the marginalized parameter median value and 1-σ range (red).

are not present in the stellar photosphere. In this work, we applied a correction to the CO abundance to account for the RLB effect.

Overall, we find a good fit to the data with a χ^2_ν =1.1 for 566 DOF and 10 free parameters. Our retrieval results are given in Extended Data Table 2 and Extended Data Fig. 4. To estimate the detection confidence of each molecule identified, we re-ran the retrieval leaving out the molecule in question and computed the detection significance using the Bayesian evidence between the models with and without the molecule. We report the results where H$_2$S and NH$_3$ are included in the model, though the G395H data are not sufficient to confidently detect either species. We report the abundances and detection significances from the ATMO results, as they can be directly used to compare against the non-equilibrium models presented in the main text.

ATMO WASP-107b Forward non-equilibrium chemistry Models

It is computationally infeasible to currently run the ATMO retrieval with the full non-equilibrium photochemistry self-consistently computed at every model evaluation 'on the fly'. Instead, we adopt a two-step grid-retrieval approach, first computing a grid of non-equilibrium chemistry values which are then fit against the retrieved VMR abundances. As we use the same ATMO model setup for both the forward and retrieval modeling, the abundances computed between them can be self-consistently compared.
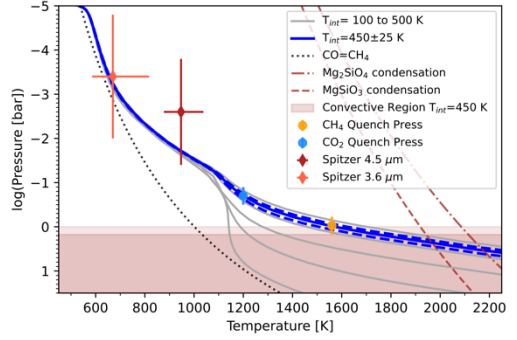
Our use of a 1D atmospheric model to interpret the non-equilibrium chemistry has several assumptions. The first is that the atmosphere can be considered 1D and is independent of both latitude and longitude.
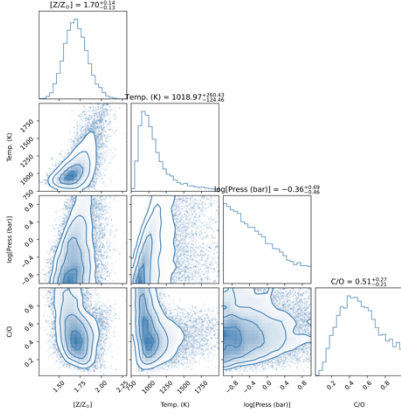
Extended Data Figure 5 Equilibrium chemistry estimation. Shown is a posterior distribution of metallicity, temperature, pressure and C/O equilibrium chemistry[88] values that are simultaneously compatible with the retrieved abundances of H_2O, CO, CO_2.


Extended Data Figure 6 Pressure-Temperature Profiles. Shown are P-T profiles in radiative-convective equilibrium with T_{int} values ranging from 100 to 500 K (grey). The T-P with the best-fit T_{int} is shown (blue), with a shaded region showing where the model is dominated by convection. The quench pressures for CO_2 and CH_4 are also depicted along with Mg-Si condensation curves (dashed, dot dashed lines). The equilibrium CH_4=CO equal abundance curve is also shown (dotted line), with the CH_4 abundance dropping at increased temperatures. The brightness temperatures measured from Spitzer secondary eclipse observations are shown from Ref.[91]. The corresponding pressures and ranges are derived from the best-fit model contribution function, with the y-axis range encapsulating 80% of the total emitted flux. The Spitzer brightness temperatures are consistent with the best-fitting T_{int} = 450K T-P profile.

Hot and ultra-hot Jupiters show large day-night temperature gradients[85]. Spitzer phase curves show these differences decrease at lower T_{eq}[86]. Thus, the latitude and longitude temperature differences for warm ~750K planets like WASP-107b are expected to be modest. Another important assumption is that the parameters of T_{int} and K_{zz} are constant and assumed to be uniform with depth. Our model contains a single convective region (see Extended Data Fig. 6), though the possibility of a separate low-pressure convective zone has been studied[87]. Multiple convective regions would affect our interpretation of T_{int} and the link between atmospheric and interior constraints. In addition, our modeling also assumes a single K_{zz} value which is constant with altitude. Theoretical studies have predicted that K_{zz} increases with altitude[13]. Higher K_{zz} values at higher altitudes would not greatly affect our results, as the quench pressures for the molecular features probed here are similar (see Extended Data Fig. 6). However, if multiple convective zones are present, the use of a single K_{zz} value may have to be re-visited.

To estimate the parameter space needed for the grid, we first used a chemical equilibrium model[88] and assumed a single quench pressure to estimate the posterior distribution of temperature, pressure, metallicity, and C/O ratio parameters that are consistent with the retrieved abundances (see Extended Data Fig. 5). This equilibrium model indicated metallicites near 50× solar, C/O ratios near 0.5 and temperatures near 1000 K at pressures just below a bar are needed to fit the observed molecular abundances. These temperatures are reached at 1 bar only if the planet has an intrinsic temperature greater than about 300 K with super-solar metalicities (see Extended Data Fig. 6). Intrinsic temperatures lower than 300 K are ruled out as CH_4 becomes be too abundant in the deep atmosphere, such that no amount of mixing could sufficiently deplete the molecule. We also estimate a limit on K_{zz} to be less than $10^{13.5}$ cm^2/s based on requiring velocities to
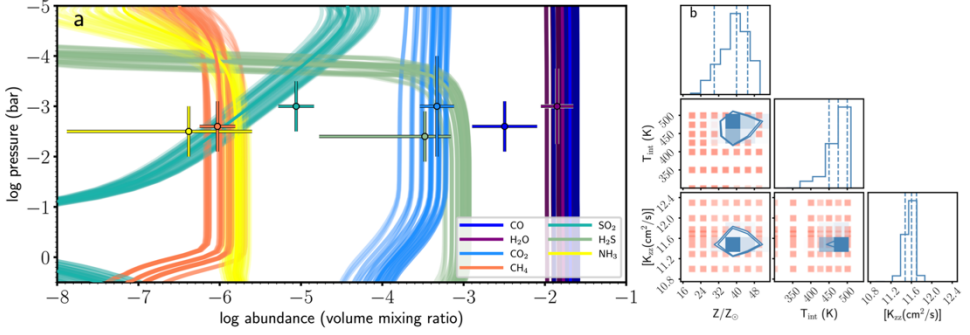
Extended Data Figure 7 WASP-107b forward non-equilibrium chemistry model grid results. (**a**) Shown are the best-fitting chemical abundances (within 1-σ) from the nonequilibrium chemistry models along with the retrieved values from the JWST transmission spectrum (datapoints). (**b**) The corner plot depicts the forward model grid points (red squares) along with the constraints in atmospheric metallicity ($Z/Z_\odot$), intrinsic temperature (T_{int}), and eddy diffusion coefficient (K_{zz}).

be less than the local sound speed. The presence of clouds near millibar pressures also places a lower limit on K_{zz} of $\sim 10^9$ cm^2/s, as significant vertical mixing is needed to keep the aerosol particles aloft[13].

We input pressure-temperature profiles in radiative-convective equilibrium, using intrinsic temperatures (T_{int}) of 300 to 500 K in steps of 50 K along with a T_{int} of 425 K. With these T-P profiles, we computed the non-equilibrium chemistry as described in Ref. [50], using metallicities (Z) between 20 and 50× solar in steps of 5×, and ten $\log_{10}[K_{zz}$ (cm^2/s)] values ranging from 11 to 13. A K6V star was used for our input to the photochemical model[89]. Each non-equilibrium model was integrated to 1×10^8 sec, which we found was sufficient such that the abundances did not evolve further. We assumed a solar C/O ratio, which is also consistent with WASP-107A from Ref. [90] who found values of C/O=0.5±0.1. We find the C/O ratio does not differ substantially from the solar or host-star value (see Extended Data Fig. 5) and we subsequently ran low (0.1 & 0.2) and high (0.7) non-equilibrium chemistry cases which did not improve the fits.

For this grid of models, we then calculated the χ^2 for each grid-model, using the retrieved abundances for H$_2$O, CO, CO$_2$, CH$_4$ and SO$_2$ in Extended Data Table 2. We did not use the H$_2$S or NH$_3$ abundances, as they are not

fully supported by the data and the errors in any case are large. The best-fit model has a good χ^2 of 4.1 when fitting the 5 abundances with 3 grid-parameters (see Fig. 3 and Extended Data Fig. 7). The grid-posterior can be seen in Extended Data Fig. 7, where each model was given a weight proportional to it's probability, P, calculated with $P = e^{-\chi^2/2}$. From the marginalized grid-posterior, we fit a Gaussian to the distributions and report the fitted $Z/Z_\odot$, T_{int} and K_{zz} values in Extended Data Table 2.

We find the molecular constraints to be highly constraining for both T_{int} and K_{zz}. Lower vertical mixing rates generally require higher intrinsic temperatures to deplete CH$_4$ to similar values. However, if T_{int} becomes too high it over-depletes CH$_4$ relative to CO$_2$. In addition, SO$_2$ helps provide an upper bound on K_{zz} as SO$_2$ is sensitive to both the photochemistry, needed to produce the species at low pressures, and vertical mixing. Higher values of K_{zz} mix the species from deeper pressures where the abundances are lower, while lower K_{zz} values allow the photochemistry to build up the species near 0.1 mbar pressures.

NEMESIS free retrievals

NEMESIS is a free-chemistry radiative transfer and retrieval code, initially developed for solar system applications[92]. It couples a
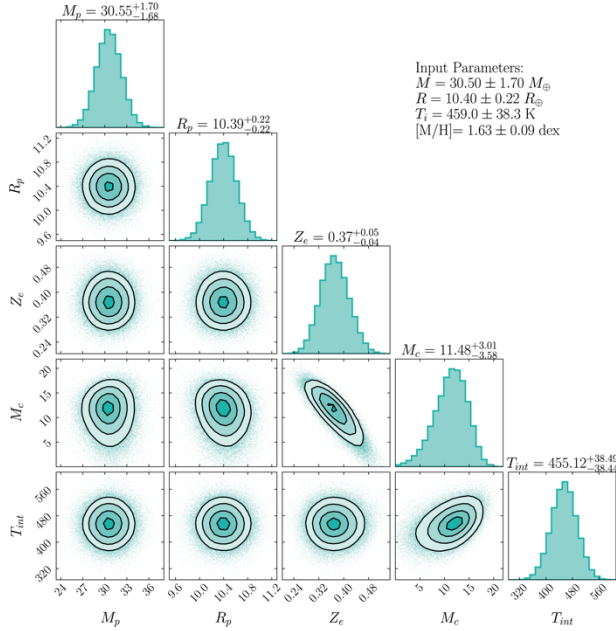
Extended Data Figure 8 Interior structure modeling constraints. A corner plot of the posterior mass (M_J)), radius (R_J), envelope metallicity (unitless), core mass ($M_\oplus$), and intrinsic temperature (K). The model inputs (from observations) are shown in the upper-right, and the priors were weakly-informative. The overall bulk metallicity is set by M, R, and T_{int}, and can be seen as an arc in Z_e-M_c space. Our atmospheric constraint restricts us to a section of this arc; without it, the two parameters would be fully degenerate, running from $M_c = 0$ on one side to $Z_e = 0$ on the other, though the effect on Z_p would be much more limited. The intrinsic temperature is significantly higher than unheated evolution models would produce and is thus evidence of tidal heating (see text).

correlated-k [56] radiative transfer scheme with the PyMultiNest [68–70, 93] Nested Sampling algorithm [94]. It has been extensively applied to spectra of hot Jupiter exoplanets (e.g. [95–97]).

The retrievals for WASP-107b incorporate abundances of the gases H_2O (line data: [98]), CO_2 [99], CO [100], CH_4 [101], SO_2 [84], NH_3 [102], HCN [103] and H_2S [104]. For each of the gas abundances, we specify a log-uniform prior spanning 10^{-12} to $10^{-0.5}$. The rest of the atmosphere is composed of H_2 and He with a ratio of 0.8547:0.1453. Collision-induced absorption for H_2 and He is taken from [105] and [106].

Other retrieved properties are an isothermal temperature with a uniform prior and a range of 300 — 1000 K, and a grey cloud top pressure with a log-uniform prior and a range of 10^{-8} — 100 bars. We also retrieve the planetary radius at a reference pressure of

100 bars. The retrieved abundances are given in Extended Data Table 2. Additional retrievals were run which had a more flexible T-P profile in addition to retrievals with patchy-clouds and enstatite clouds, though were not favored statistically over the simpler model.

Interior Structure Models

The constraints we found for the intrinsic temperature of WASP-107 b have important implications for the interior structure of the planet. To investigate these, we use the interior structure models of Ref. [39], updated to use the H/He EOS[107] and parameterize the amount of metal in the core vs mixed into the envelope. As in Ref. [39], we assume the metal is a 50-50 mixture of rock and ice.

To match our models to WASP-107 b, we use a Bayesian retrieval approach similar to the one used in Ref. [108]. However, our measurement of T_{int} determines the thermal

state of the plane rather than thermal evolution. The parameters of the statistical model were therefore the mass of the planet M, the metallicity of the envelope Z_e (a mass fraction), the core mass M_c, and the specific entropy of the envelope s. From these, our forward model calculates the radius and T_{int} of the planet. The model was constrained by four normally-distributed observations: the mass, the radius, the atmospheric metallicity, and T_{int}. These are constraining enough that we can choose very uninformative priors just to keep the parameters inside model bounds: a uniform mass prior from 0.01 to 30 M_J, a uniform Z_{env} from 0 to 1, a uniform core mass from 0 to M_J (thus conditional on M but still proper), and a uniform entropy prior from 5 to 11 k_b/ baryon. We sampled from the posterior using the Metropolis-Hastings MCMC algorithm and verified convergence with the auto-correlation plots and the Gelman-Rubin statistic[109].

Our interior model retrievals (See Extended Data Fig. 8) find a planet that contains similar amounts of H/He vs heavier elements, with $Z_p = 0.608 \pm 0.046$. This seems reasonable for a planet of this mass: it accreted a substantial amount of material from the disk, but never reached the runaway gas accretion stage. However, this is in stark contrast to previous estimates of the planet's composition, which saw it as having substantially larger quantities of H/He: > 85% H/He from Ref. [10]! The reason is that our measured T_{int} is much hotter than a standard thermal evolution model would suggest; we would expect the planet to have cooled below our 2σ lower bound of 300 K within tens of Myr. of formation. Instead, it is clear that the planet is being inflated by an extra heat source despite being too cool to experience hot Jupiter-type inflation[110]. Instead, a mechanism such as tidal heating[111,112,113], previously suspected to be operating on WASP-107 b[10, 114], is warming the interior. These models propose that the eccentricity of WASP-107 b is excited by WASP-107 c, but then damped out through tidal interaction

with the star; the resulting energy is deposited in the interior of the planet. Our large measured T_{int} is evidence that this process could be occurring, with a precise eccentricity further capable of constraining the mechanism.

Another interesting result of our interior structure models is that it puts constraints on the mass of the planet's core. The mass, radius, and T_{int} already constrain the overall metallicity of the planet (more metal means a smaller planet) to $Z_p=63.5^{+10.4}_{-8.5}$%, but we also have a measurement of the atmospheric metallicity of the planet. This allows us to make a modestly better constraint on Z (see previous paragraph); more importantly, metal seen in the bulk but not in the atmosphere must be hidden in the interior in a core or composition layers [see Ref 108, for further discussion]. Assuming a uniform composition core gives us $M_c = 11.5^{+3.0}_{-3.6} M_\oplus$. Importantly, this range excludes zero, meaning that we have detected the presence of a core! The exact structure of the interior may not be exactly an envelope-on-core model, but may be more like Neptune and Uranus with a rocky core, water envelope, then a H/He envelope[36]. Alternatively, the core may be diffuse and/or layered as Jupiter's is thought to be[37, 38]. Nevertheless, our result that a core exists is not affected by these possibilities: one cannot propose a layered core without a core in the first place.

Data availability

The data used in this paper are associated with JWST program GO 1224 (PI Birkmann) and are publicly available from the Mikulski Archive for Space Telescopes (https://mast.stsci.edu) from 23 June 2024. The data products in Figures 1, 2, 3 are available here: https://doi.org/10.5281/zenodo.10891400.

Code availability

The codes used in this publication to extract, reduce, and analyze the data are as follows; STScI JWST Calibration pipeline (https://github.com/spacetelescope/jwst), FIREFLy[22, 42] And TEATRO (https://github.com/ncrouzet/TEATRO). In

addition, these made use ExoTiC-LD[120] (https://exotic-ld.readthedocs.io/en/latest/), Emcee (https://emcee.readthedocs.io/en/stable/)[121], which uses the python libraries scipy[122] numpy[123] astropy[124] and matplotlib[125]. Model and retrievals were generated using ATMO, a proprietary code extensively described in Refs. [20, 47, 48, 49, 50, 51], and NEMESIS[92] (https://github.com/nemesiscode/radtrancode).

Additional Information
Correspondence and requests for materials should be addressed to David K. Sing (dsing@jhu.edu).

[42] Rustamkulov, Z., Sing, D. K., Liu, R. & Wang, A. Analysis of a JWST NIRSpec Lab Time Series: Characterizing Systematics, Recovering Exoplanet Transit Spectroscopy, and Constraining a Noise Floor. *Astrophys. J. L.* **928**, L7 (2022).

[43] Kipping, D. M. Efficient, uninformative sampling of limb darkening coefficients for two-parameter laws. *Mon. Not. R. Astron. Soc.* **435**, 2152–2160 (2013).

[44] Magic, Z., Chiavassa, A., Collet, R. & Asplund, M. The Stagger-grid: A grid of 3D stellar atmosphere models. IV. Limb darkening coefficients. *Astron. Astrophys.* **573**, A90 (2015).

[45] Dai, F. & Winn, J. N. The Oblique Orbit of WASP-107b from K2 Photometry. *Astron. J.* **153**, 205 (2017).

[46] Deming, D. & Sheppard, K. Spectral Resolution-linked Bias in Transit Spectroscopy of Extrasolar Planets. *Astrophys. J. L.* **841**, L3 (2017).

[47] Amundsen, D. S. *et al.* Accuracy tests of radiation schemes used in hot Jupiter global circulation models. *Astron. Astrophys.* **564**, A59 (2014).

[48] Tremblin, P. *et al.* Fingering Convection and Cloudless Models for Cool Brown Dwarf Atmospheres. *Astrophys. J. L.* **804**, L17 (2015).

[49] Tremblin, P. *et al.* Cloudless Atmospheres for L/T Dwarfs and Extrasolar Giant Planets. *Astrophys. J. L.* **817**, L19 (2016).

[50] Drummond, B. *et al.* The effects of consistent chemical kinetics calculations on the pressure-temperature profiles and emission spectra of hot Jupiters. *Astron. Astrophys.* **594**, A69 (2016).

[51] Goyal, J. M. *et al.* A library of ATMO forward model transmission spectra for hot Jupiter exoplanets. *Mon. Not. R. Astron. Soc.* **474**, 5158–5185 (2018).

[52] Edwards, J. M. & Slingo, A. Studies with a flexible new radiation code. I: Choosing a configuration for a large-scale model. *Quarterly Journal of the Royal Meteorological Society* **122**, 689–719 (1996).

[53] Baudino, J. L. *et al.* Interpreting the photometry and spectroscopy of directly imaged planets: a new atmospheric model applied to β Pictoris b and SPHERE observations. *Astron. Astrophys.* **582**, A83 (2015).

[54] Mollière, P., van Boekel, R., Dullemond, C., Henning, T. & Mordasini, C. Model Atmospheres of Irradiated Exoplanets: The Influence of Stellar Parameters, Metallicity, and the C/O Ratio. *Astrophys. J.* **813**, 47 (2015).

[55] Baudino, J.-L. *et al.* Toward the Analysis of JWST Exoplanet Spectra: Identifying Troublesome Model Parameters. *Astrophys. J.* **850**, 150 (2017).

[56] Lacis, A. A. & Oinas, V. A description of the correlated-k distribution method for modelling nongray gaseous absorption, thermal emission, and multiple scattering in vertically inhomogeneous atmospheres. *J. Geophys. Res.* **96**, 9027–9064 (1991).

[57] Goyal, J. M. *et al.* A library of ATMO forward model transmission spectra for hot Jupiter

exoplanets. *Mon. Not. R. Astron. Soc.* **474**, 5158–5185 (2018).

[58] Goyal, J. M. *et al.* A library of self-consistent simulated exoplanet atmospheres. *Mon. Not. R. Astron. Soc.* **498**, 4680–4704 (2020).

[59] Gordon, S. & McBride, B. J. Computer program for calculation of complex chemical equilibrium compositions and applications. part 1: Analysis. *NASA Reference Publication* **1311** (1994) .

[60] McBride, B. J. Coefficients for calculating thermodynamic and transport properties of individual species. *National Aeronautics and Space Administration, Office of Management, Scientific and Technical Information Program* **4513** (1993) .

[61] Asplund, M., Grevesse, N., Sauval, A. J. & Scott, P. The Chemical Composition of the Sun. *Annu. Rev. Astron.* **47**, 481–522 (2009).

[62] Caffau, E., Ludwig, H. G., Steffen, M., Freytag, B. & Bonifacio, P. Solar Chemical Abundances Determined with a CO5BOLD 3D Model Atmosphere. *Sol. Phys.* **268**, 255–269 (2011).

[63] Goyal, J. M. *et al.* Fully scalable forward model grid of exoplanet transmission spectra. *Mon. Not. R. Astron. Soc.* **482**, 4503–4513 (2019).

[64] Venot, O. *et al.* A chemical model for the atmosphere of hot Jupiters. *Astron. Astrophys.* **546**, A43 (2012).

[65] Tsai, S.-M. *et al.* A Comparative Study of Atmospheric Chemistry with VULCAN. *Astrophys. J.* **923**, 264 (2021).

[66] Venot, O. *et al.* New chemical scheme for giant planet thermochemistry. Update of the methanol chemistry and new reduced chemical scheme. *Astron. Astrophys.* **634**, A78 (2020).

[67] Lecavelier Des Etangs, A., Pont, F., Vidal-Madjar, A. & Sing, D. Rayleigh scattering in the transit spectrum of HD 189733b. *Astron. Astrophys.* **481**, L83–L86 (2008).

[68] Feroz, F. & Hobson, M. P. Multimodal nested sampling: an efficient and robust alternative to Markov Chain Monte Carlo methods for astronomical data analyses. *MNRAS* **384**, 449–463 (2008).

[69] Feroz, F., Hobson, M. P. & Bridges, M. MULTINEST: an efficient and robust Bayesian inference tool for cosmology and particle physics. *MNRAS* **398**, 1601–1614 (2009).

[70] Feroz, F., Hobson, M. P., Cameron, E. & Pettitt, A. N. Importance Nested Sampling and the MultiNest Algorithm. *Open J. of Astrophysics* **2**, 10 (2019).

[71] Evans, T. M. *et al.* An ultrahot gas-giant exoplanet with a stratosphere. *Nature* **548**, 58–61 (2017).

[72] Wakeford, H. R. *et al.* HAT-P-26b: A Neptune-mass exoplanet with a well-constrained heavy element abundance. *Science* **356**, 628–631 (2017).

[73] Spake, J. J. *et al.* Helium in the eroding atmosphere of an exoplanet. *Nature* **557**, 68–70 (2018).

[74] Nikolov, N. *et al.* An absolute sodium abundance for a cloud-free 'hot Saturn' exoplanet. *Nature* **557**, 526–529 (2018).

[75] Carter, A. L. *et al.* Detection of Na, K, and H_2O in the hazy atmosphere of WASP-6b. *Mon. Not. R. Astron. Soc.* **494**, 5449–5472 (2020).

[76] Line, M. R. *et al.* Information Content of Exoplanetary Transit Spectra: An Initial Look. *Astrophys. J.* **749**, 93 (2012).

[77] Guillot, T. On the radiative equilibrium of irradiated planetary atmospheres. *Astron. Astrophys.* **520**, A27 (2010).

[78] Barber, R. J., Tennyson, J., Harris, G. J. & Tolchenov, R. N. A highaccuracy computed water line list. *Mon. Not. R. Astron. Soc.* **368**, 1087– 1094 (2006).

[79] Tashkun, S. & Perevalov, V. Cdsd-4000: High-resolution, hightemperature carbon dioxide spectroscopic databank. *Journal of Quantitative Spectroscopy and Radiative Transfer* **112**, 1403–1410 (2011).

[80] Rothman, L. *et al.* Hitemp, the high-temperature molecular spectroscopic database. *Journal of Quantitative Spectroscopy and Radiative Transfer* **111**, 2139–2150 (2010). xVIth Symposium on High Resolution Molecular Spectroscopy (HighRus-2009) .

[81] Yurchenko, S. N. & Tennyson, J. ExoMol line lists – IV. The rotation–vibration spectrum of methane up to 1500 K. *Monthly Notices of the Royal Astronomical Society* **440**, 1649–1661 (2014).

[82] Yurchenko, S. N., Barber, R. J. & Tennyson, J. A variationally computed line list for hot NH_3. *Mon. Not. R. Astron. Soc.* **413**, 1828–1834 (2011).

[83] Rothman, L. *et al.* The hitran2012 molecular spectroscopic database. *Journal of Quantitative Spectroscopy and Radiative Transfer* **130**, 4–50 (2013).

[84] Underwood, D. S. *et al.* ExoMol molecular line lists - XIV. The rotationvibration spectrum of hot SO_2. *Mon. Not. R. Astron. Soc.* **459**, 3890–3899 (2016).

[85] Mikal-Evans, T. *et al.* Diurnal variations in the stratosphere of the ultrahot giant exoplanet WASP-121b. *Nature Astronomy* **6**, 471–479 (2022).

[86] Bell, T. J. *et al.* A comprehensive reanalysis of Spitzer's 4.5 μm phase curves, and the phase variations of the ultra-hot Jupiters MASCARA-1b and KELT-16b. *Mon. Not. R. Astron. Soc.* **504**, 3316–3337 (2021).

[87] Guillot, T. & Showman, A. P. Evolution of "51 Pegasus b-like" planets. *Astron. Astrophys.* **385**, 156–165 (2002).

[88] Cubillos, P., Blecic, J. & Fossati, L. Radiative and Chemical Equilibrium Calculations with Application to Exoplanets. *journal* (2022) .

[89] France, K. *et al.* The MUSCLES Treasury Survey. I. Motivation and Overview. *Astrophys. J.* **820**, 89 (2016).

[90] Hejazi, N. *et al.* Elemental Abundances of the Super-Neptune WASP107b's Host Star Using High-resolution, Near-infrared Spectroscopy. *Astrophys. J.* **949**, 79 (2023).

[91] Deming, D. *et al.* Emergent Spectral Fluxes of Hot Jupiters: An Abrupt Rise in Dayside Brightness Temperature Under Strong Irradiation. *Astron. J.* **165**, 104 (2023).

[92] Irwin, P. G. J. *et al.* The NEMESIS planetary atmosphere radiative transfer and retrieval tool. *JQSRT* **109**, 1136–1150 (2008).

[93] Buchner, J. *et al.* X-ray spectral modelling of the AGN obscuring region in the CDFS: Bayesian model selection and catalogue. *Astron. Astrophys.* **564**, A125 (2014).

[94] Krissansen-Totton, J., Garland, R., Irwin, P. & Catling, D. C. Detectability of Biosignatures in Anoxic Atmospheres with the James Webb Space Telescope: A TRAPPIST-1e Case Study. *AJ* **156**, 114 (2018).

[95] Barstow, J. K., Aigrain, S., Irwin, P. G. J. & Sing, D. K. A Consistent Retrieval Analysis of 10 Hot Jupiters Observed in Transmission. *Astrophys. J.* **834**, 50 (2017).

[96] Lewis, N. K. *et al.* Into the UV: The Atmosphere of the Hot Jupiter HAT-P-41b Revealed. *ApJL* **902**, L19 (2020).

[97] Rathcke, A. D. *et al.* HST PanCET Program: A Complete Near-UV to Infrared Transmission Spectrum for the Hot Jupiter WASP-79b. *AJ* **162**, 138 (2021).

[98] Polyansky, O. L. *et al.* ExoMol molecular line lists XXX: a complete highaccuracy line list for water. *Mon. Not. R. Astron. Soc.* **480**, 2597–2608 (2018).

[99] Yurchenko, S. N., Mellor, T. M., Freedman, R. S. & Tennyson, J. ExoMol line lists - XXXIX. Ro-vibrational molecular line list for CO_2. *MNRAS* **496**, 5282–5291 (2020).

[100] Li, G. *et al.* Rovibrational Line Lists for Nine Isotopologues of the CO Molecule in the X $^1\Sigma^+$ Ground Electronic State. *Astrophys. J. S.* **216**, 15 (2015).

[101] Yurchenko, S. N., Amundsen, D. S., Tennyson, J. & Waldmann, I. P. A hybrid line list for CH_4 and hot methane continuum. *Astron. Astrophys.* **605**, A95 (2017).

[102] Coles, P. A., Yurchenko, S. N. & Tennyson, J. ExoMol molecular line lists - XXXV. A rotation-vibration line list for hot ammonia. *Mon. Not. R. Astron. Soc.* **490**, 4638–4647 (2019).

[103] Barber, R. J. *et al.* ExoMol line lists - III. An improved hot rotationvibration line list for HCN and HNC. *MNRAS* **437**, 1828–1835 (2014).

[104] Azzam, A. A. A., Tennyson, J., Yurchenko, S. N. & Naumenko, O. V. ExoMol molecular line lists – XVI. The rotation–vibration spectrum of hot H2S. *Monthly Notices of the Royal Astronomical Society* **460**, 4063–4074 (2016).

[105] Borysow, A., Jorgensen, U. G. & Fu, Y. High-temperature (1000-7000 K) collision-induced absorption of H"2 pairs computed from the first principles, with application to cool and dense stellar atmospheres. *J. Quant. Spectrosc. Radiat. Transf.* **68**, 235–255 (2001).

[106] Borysow, A. Collision-induced absorption coefficients of H_2 pairs at temperatures from 60 K to 1000 K. *A&A* **390**, 779–782 (2002).

[107] Chabrier, G., Mazevet, S. & Soubiran, F. A New Equation of State for Dense Hydrogen-Helium Mixtures. *Astrophys. J.* **872**, 51 (2019).

[108] Thorngren, D. & Fortney, J. J. Connecting Giant Planet Atmosphere and Interior Modeling: Constraints on Atmospheric Metal Enrichment. *Astrophys. J. L.* **874**, L31 (2019).

[109] Gelman, A. & Rubin, D. B. Inference from Iterative Simulation Using Multiple Sequences. *Statistical Science* **7**, 457–472 (1992).

[110] Miller, N. & Fortney, J. J. The Heavy-element Masses of Extrasolar Giant Planets, Revealed. *Astrophys. J. L.* **736**, L29 (2011).

[111] Bodenheimer, P. & Lin, D. N. C. Implications of Extrasolar Planets for Understanding Planet Formation. *Annual Review of Earth and Planetary Sciences* **30**, 113–148 (2002).

[112] Jackson, B., Greenberg, R. & Barnes, R. Tidal Heating of Extrasolar Planets. *Astrophys. J.* **681**, 1631–1638 (2008).

[113] Millholland, S. Tidally Induced Radius Inflation of Sub-Neptunes. *Astrophys. J.* **886**, 72 (2019).

[114] Millholland, S., Petigura, E. & Batygin, K. Tidal Inflation Reconciles Low-density Sub-Saturns with Core Accretion. *Astrophys. J.* **897**, 7 (2020).

[115] JWST calibration pipeline developers. jwst: Python library for science observations from the James Webb Space Telescope (2022). URL https://github.com/spacetelescope/jwst.

[116] CRDS developers. CRDS: Calibration Reference Data System for HST and JWST (2022). URL https://github.com/spacetelescope/crds.

[117] Foreman-Mackey, D. *et al.* exoplanet: Gradient-based probabilistic inference for exoplanet data & other astronomical time series. *arXiv e-prints* arXiv:2105.01994 (2021).

[118] Foreman-Mackey, D. *et al.* exoplanet-dev/exoplanet v0.5.1 Zenodo (2021).

[119] Morello, G. *et al.* The ExoTETHyS Package: Tools for Exoplanetary Transits around Host Stars. *Astron. J.* **159**, 75 (2020).

[120] Grant, D. & Wakeford, H. R. Exo-TiC/ExoTiC-LD: ExoTiC-LD v3.0.0. Zenodo (2022).

[121] Foreman-Mackey, D., Hogg, D. W., Lang, D. & Goodman, J. emcee: The MCMC Hammer. *Publ. Astron. Soc. Pacif.* **125**, 306 (2013).

[122] Virtanen, P. *et al.* SciPy 1.0: Fundamental Algorithms for Scientific Computing in Python. *Nature Methods* **17**, 261–272 (2020).

[123] Harris, C. R. *et al.* Array programming with NumPy. *Nature* **585**, 357–362 (2020).

[124] Astropy Collaboration *et al.* The Astropy Project: Building an Open science Project and Status of the v2.0 Core Package. *Astron. J.* **156**, 123 (2018).

[125] Hunter, J. D. Matplotlib: A 2d graphics environment. *Computing in Science & Engineering* **9**, 90–95 (2007).